Inorganic Chemistry

Soft Chemical Control of Superconductivity in Lithium Iron Selenide Hydroxides Li$_{1-x}$Fe$_x$(OH)Fe$_{1-y}$Se

Hualei Sun,[†,‡] Daniel N. Woodruff,[†] Simon J. Cassidy,[†,§] Genevieve M. Allcroft,[†] Stefan J. Sedlmaier,[†] Amber L. Thompson,[†] Paul A. Bingham,[∥] Susan D. Forder,[∥] Simon Cartenet,[∥] Nicolas Mary,[∥] Silvia Ramos,[⊥] Francesca R. Foronda,[#] Benjamin H. Williams,[#] Xiaodong Li,[‡] Stephen J. Blundell,[#] and Simon J. Clarke*,[†]

[†]Department of Chemistry, Inorganic Chemistry Laboratory, University of Oxford, South Parks Road, Oxford, OX1 3QR, U.K.

[‡]Beijing Synchrotron Radiation Facility, Institute of High Energy Physics, Chinese Academy of Science, Beijing 100049, China

[§]Harwell Science and Innovation Campus, Diamond Light Source Ltd., Didcot, OX11 0DE, U.K.

[∥]Materials and Engineering Research Institute, Faculty of Arts, Computing, Engineering and Sciences, Sheffield Hallam University, City Campus, Howard Street, Sheffield, S1 1WB, U.K.

[⊥]School of Physical Sciences, Ingram Building, University of Kent, Canterbury, Kent, CT2 7NH, U.K.

[#]Department of Physics, Clarendon Laboratory, University of Oxford, Parks Road, Oxford, OX1 3PU, U.K.

ⓢ *Supporting Information*

ABSTRACT: Hydrothermal synthesis is described of layered lithium iron selenide hydroxides Li$_{1-x}$Fe$_x$(OH)Fe$_{1-y}$Se ($x \sim 0.2$; $0.02 < y < 0.15$) with a wide range of iron site vacancy concentrations in the iron selenide layers. This iron vacancy concentration is revealed as the only significant compositional variable and as the key parameter controlling the crystal structure and the electronic properties. Single crystal X-ray diffraction, neutron powder diffraction, and X-ray absorption spectroscopy measurements are used to demonstrate that superconductivity at temperatures as high as 40 K is observed in the hydrothermally synthesized samples when the iron vacancy concentration is low ($y < 0.05$) and when the iron oxidation state is reduced slightly below +2, while samples with a higher vacancy concentration and a correspondingly higher iron oxidation state are not superconducting. The importance of combining a low iron oxidation state with a low vacancy concentration in the iron selenide layers is emphasized by the demonstration that reductive postsynthetic lithiation of the samples turns on superconductivity with critical temperatures exceeding 40 K by displacing iron atoms from the Li$_{1-x}$Fe$_x$(OH) reservoir layer to fill vacancies in the selenide layer.
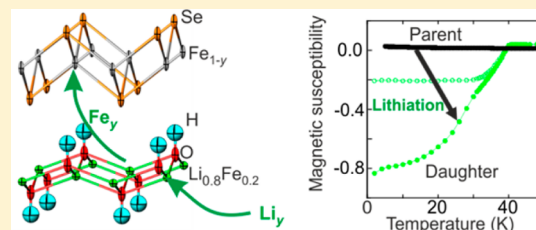
INTRODUCTION

Iron-based arsenide[1] and selenide superconductors are compounds where chemical control of the properties by isovalent or aliovalent substitution[1−4] reveals competing itinerant antiferromagnetic and unconventional superconducting states.[5,6] The almost-stoichiometric tetragonal polymorph of iron selenide, Fe$_{1.01}$Se, is a superconductor with a superconducting transition temperature T_c of 8.5 K.[7,8] Some FeSe derivatives exhibit higher T_cs[9] but often contain ordered arrays of iron site vacancies,[10,11] with superconductivity in minority regions.[12−14] In order to decrease the concentration of iron site vacancies in the FeSe layers, stoichiometric, super-conducting FeSe itself has been used in the synthesis, at ambient temperatures and below, of intercalates using solutions of electropositive metals in ammonia.[15] These intercalates, which often superconduct at temperatures as high as 45 K, contain variable electropositive metal and ammonia and amide contents and are the subject of current investigation.[16−19]

Recently layered lithium iron selenide hydroxides have been reported with T_cs of up to about 40 K.[20−22] Here we reveal the phase width in these hydrothermally synthesized compounds Li$_{1-x}$Fe$_x$(OH)Fe$_{1-y}$Se ($x \sim 0.2$; $0.02 < y < 0.15$) and control their compositions. We quantify the correlations between superconductivity and the concentration of iron vacancies in the selenide layer and the electron count of iron. We underline this by demonstrating that postsynthetic reductive lithiation displaces iron ions from the hydroxide layer "reservoir" into the selenide layer to reduce the iron deficiency in the selenide layers to zero and turn on bulk superconductivity with $T_c > 40$ K.

EXPERIMENTAL METHODS

Synthesis. The hydrothermal synthesis was adapted from that in ref 20. Our approach differs from that previously reported in that we used tetragonal FeSe as the source of all the Se and most of the Fe in the synthesis. The Pourbaix diagram for iron and selenium is known from investigations of the contamination of natural waters[23] and
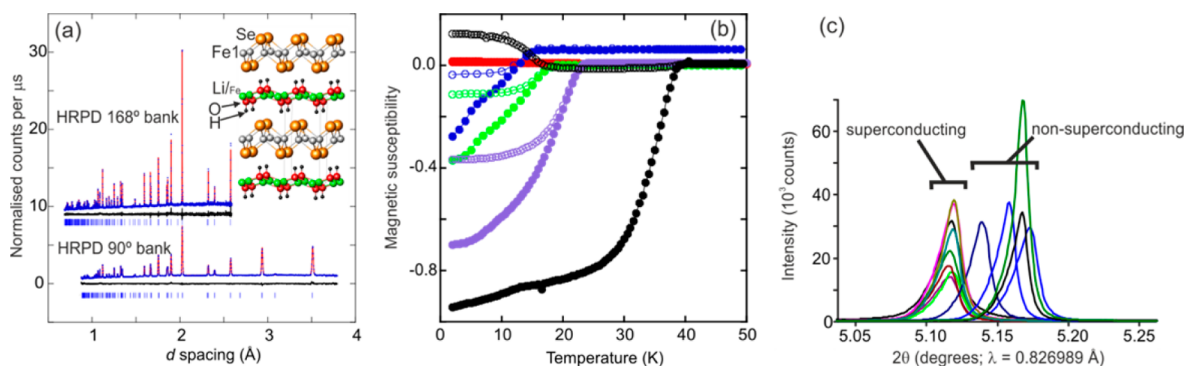
Figure 1. (a) The structure of the lithium iron selenide hydroxides and a typical refinement against neutron diffraction data (HRPD at ISIS) showing data (blue dots), calculated (red line), difference (black line), and reflection positions. Data for the 168° bank have been displaced by 9 units along the vertical axis. $Li_{1-x}Fe_x(OH)Fe_{1-y}Se$: space group $P4/nmm$ (No. 129), $a \sim 3.8$ A, $c \sim 9.2$ Å. Atomic positions (origin choice 2: inversion center at origin): Fe, site $2a$ (1/4, 3/4, 0); Se, site $2c$ (3/4, 3/4, $z \sim 0.16$); O, site $2c$ (1/4, 1/4, $z \sim 0.43$); $Li_{1-x}Fe_x$, site $2b$ (3/4, 1/4, 1/2); H, site $2c$ (1/4, 1/4, $z \sim 0.33$) (see Tables S1 and S2, Figures S1 and S2, and the crystallographic information file included in the Supporting Information). (b) Magnetic susceptibility measurements showing the full range of behavior spanned by hydrothermally synthesized samples. Zero-field-cooled (filled symbols) and field-cooled (open symbols) data are shown. Some samples showed a high normal state background due to minuscule amounts of magnetic impurities. The sample with the highest T_c exhibits diamagnetism in the field-cooled measurement, but also shows a low temperature transition below 20 K which is presumed to arise from a magnetic impurity present at levels below the detection limit of our diffraction experiments. SI conventions were used in determining the dimensionless magnetic susceptibility. (c) Plot of the 001 reflection measured for a range of samples on I11 showing the correlation between the c lattice parameter and whether the compounds are superconducting. The values of the basal lattice parameter a spanned a range of 0.9%, and the values of the lattice parameter c spanned a range of 1.1%. Small values of a corresponded to large values of c, so the unit cell volumes spanned just 0.8%.

reveals that under reducing conditions and at high pH values the formation of H_2Se is suppressed and FeSe is stable. Accordingly the samples were synthesized under mildly reducing and extremely basic hydrothermal conditions obtained by incorporating high purity elemental iron into the syntheses along with FeSe, using a large excess of lithium hydroxide, and by excluding oxygen from the synthesis. Typically 6 mmol (0.8 g) of tetragonal FeSe (synthesized from the elements (Fe ALFA 99.998%; Se ALFA 99.999%) as described previously[8]), 140 mmol (6 g) of $LiOH·H_2O$ (Aldrich 98%), and 5 mL of deionized and deoxygenated water were loaded into a Teflon-lined steel autoclave of 18 cm³ capacity together with variable amounts of additional iron powder. The autoclaves were tightly sealed and placed in a chamber furnace. The furnace was heated to 200 °C at 1 °C per minute, and the temperature was maintained for 12 days. The furnace was then turned off and allowed to cool naturally, and the autoclaves were removed at room temperature. The autoclaves were opened in an argon-filled glovebag, and the products were loaded into Schlenk tubes and washed three times with deionized and deoxygenated water to remove soluble side products. Magnetic impurities were removed from some syntheses using a strong magnet. The samples were dried under vacuum and removed to an argon-filled glovebox. The synthesis was scalable in the 18 cm³ autoclaves to produce 10 g of product by increasing the amount of FeSe and Fe in the synthesis 12-fold, increasing the amount of water to 7 cm³, and maintaining the amount of $LiOH·H_2O$ which remains in a large excess. Some of these samples were subsequently subjected to lithiation in which the powders were stirred in solutions of lithium in liquid ammonia at −30 °C using a Schlenk line, with subsequent evaporation of the solvent and evacuation to yield the dried product, which contained some $LiNH_2$ arising from decomposition of the Li/NH_3 solution. (*CAUTION: Ammonia has a vapor pressure of ~8 bar at ambient temperature and is highly toxic and flammable. The reactions with metal/ammonia solutions were performed in a fume hood. Pressure relief, via a mercury bubbler, for evaporating ammonia and any hydrogen formed in the reactions was always available.*)

Diffraction Measurements. X-ray powder diffraction (XRPD) measurements used beamline I11 at the Diamond Light Source, U.K., with 0.8 Å X-rays and the multianalyzer crystal detector bank. Neutron powder diffraction (NPD) measurements used the GEM and HRPD diffractometers at the ISIS Facility, U.K. Single crystal X-ray diffraction (SCXRD) was carried out on small (~10 × 10 × 1 μm) crystals

(Figure S6 in the Supporting Information) using beamline I19 at Diamond using 0.68890 Å X-rays. *Ab initio* structure solution from SCXRD data was performed using SuperFlip[24] implemented within CRYSTALS,[25] with refinements performed using CRYSTALS. Refinements against powder diffraction data (Table S1 in the Supporting Information; Figure 1; Figures S2 and S3 in the Supporting Information) were conducted using TOPAS Academic.[26]

Magnetometry. Measurements used Quantum Design MPMS SQUID magnetometers and measuring fields of 20−50 Oe to characterize the superconducting state and up to 7 T to probe the normal state susceptibilities. Samples were sequestered from air in gelatin capsules. Susceptibilities were corrected for the effect of demagnetizing fields arising from the shape of the sample.[27]

X-ray Absorption Spectroscopy. Measurements were conducted in transmission mode on beamline B18 at Diamond with the samples sequestered from air and diluted with cellulose powder. All spectra were calibrated against an iron foil. The data were analyzed using Athena and Artemis, part of the Demeter software package.[28]

Muon-Spin Rotation Spectroscopy. 300 mg of powder was contained in a silver foil packet and was sequestered from air prior to loading into the helium atmosphere of the cryostat. Variable temperature measurements were carried out in applied transverse magnetic fields of up to 30 mT on the MuSR beamline at the ISIS facility.

■ RESULTS AND DISCUSSION

Hydrothermally Synthesized Samples. The products of the hydrothermal reactions were black with metallic luster and were examined with no further synthetic treatment. SQUID magnetometry (Figure 1b) carried out on samples from iron-rich syntheses (overall ratio of Fe:Se in the synthesis of 1.16:1; i.e., 1 mmol of additional Fe for 6 mmol of FeSe in the autoclave) revealed superconductivity with T_cs in the range 10−39 K and variable shielding fractions. The use of smaller amounts of additional Fe (0 or 0.5 mmol of Fe per 6 mmol of FeSe) produced non-superconducting products. The use of larger amounts of additional Fe led to significant contamination by iron oxide side products. The products were highly crystalline and appeared single phase using high resolution X-

ray and neutron powder diffraction (Figure 1). Diffractograms were indexed on tetragonal cells in space group $P4/nmm$ with lattice parameters of $a \sim 3.8$ Å and $c \sim 9.2$ Å. Lattice parameters were found to be highly sample dependent and correlated with the occurrence, or not, of superconductivity (Figure 1c; Tables S1 and S2 in the Supporting Information): superconductors from iron-rich syntheses had unit cell volumes <133.2 Å^3 and $c/a > 2.43$, while non-superconductors from iron-poor syntheses had cell volumes >133.2 Å^3 and $c/a < 2.43$. *Ab initio* structure solution from SCXRD data yielded the chemically unsatisfactory structural model of ref 20 with iron selenide layers separated by "spacer" layers with a similar topology and with the atoms in this "spacer" layer (O and Li/$_{Fe}$ in Figure 1a) all appearing isoelectronic with oxygen. The shortest distances between the selenide ions and the nearest atoms (labeled O in Figure 1a) in the "spacer" layer were 3.62 Å, only marginally shorter than the interlayer Se⋯Se distances of 3.71 Å in tetragonal FeSe[8] and marginally longer than the between-layer Se⋯Se distance of 3.58 Å in TiSe$_2$,[29] and thus longer than one would expect for Se⋯O nonbonded distances.

NPD data collected on bulk samples enabled a chemically sensible model to be obtained. The sites labeled Li/$_{Fe}$ in the "spacer" layers were approximately null scattering, and an additional region with a negative scattering density, corresponding to a hydrogen nucleus with full occupancy within the experimental uncertainty, was located about 1 Å from the atoms in the "spacer" layers labeled as O in Figure 1a.

Two samples were measured on the GEM neutron diffractometer at room temperature and 50 K. The refinements against data gathered at the two temperatures produced similar site occupancies showing that the wide d-spacing range available on the time-of-flight diffractometer, the high crystallinity, and the almost flat neutron form factor minimize parameter correlations in the refinements against these highly crystalline samples, and that this method is robust for determining site occupancy factors with a high precision. Single crystals extracted from several of the samples measured by NPD at room temperature were found to faithfully represent the bulk of the sample probed in the NPD experiments, and the results of the refinements against all of our I19 SCXRD data sets are therefore also included in the analysis (Table S2 in the Supporting Information).

For our wide range of different samples NPD and SCXRD together produced an unambiguous structural model with lithium/iron hydroxide layers containing a 0.8:0.2 Li:Fe disordered mixture (approximately null scattering for neutrons ($b_{Li} = -1.90$ fm; $b_{Fe} = 9.45$ fm)[30] and with an average electron count similar to that of oxygen) separating iron selenide layers (Figure 1a). While we were performing this work, this conclusion was reported by other groups, each from analysis of a single composition.[21,22] Using our synthetic method, we obtained refined compositions Li$_{1-x}$Fe$_x$(OH)Fe$_{1-y}$Se with $x \sim$ 0.2, and almost sample invariant (Figure 2a), and y representing a 2−15% deficiency on the Fe1 site in the iron selenide layers. The Fe1 deficiency was similar within the uncertainty when measured using both NPD and SCXRD measurements on several sample batches spanning the range of lattice parameters, which suggests that in the samples described here it is a true deficiency and not the result of Li and Fe also sharing a vacancy-free site in the selenide layers as has been proposed in the analysis, by single crystal X-ray diffraction, of a single related composition examined elsewhere.[22] Further evidence that the iron site in the selenide layers in our samples carries a
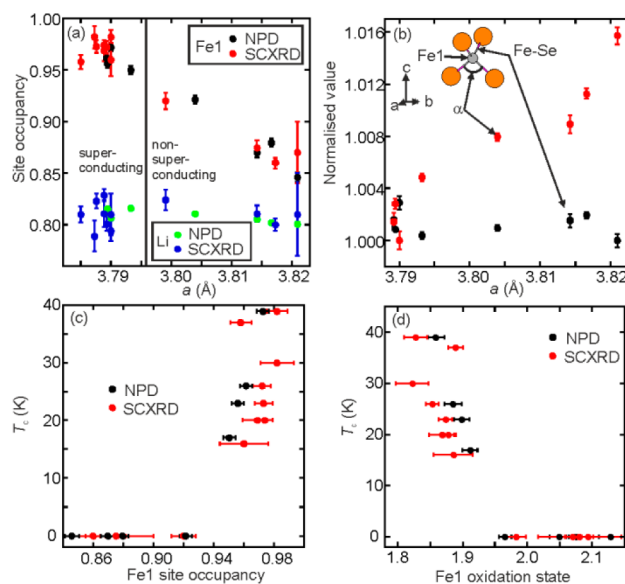

Figure 2. (a) Plot of basal lattice parameter, a, against site occupancy of Fe in the iron selenide layer and of Li in the hydroxide layer obtained from refinements against NPD and SCXRD data. Lattice parameters for the SCXRD samples were obtained at ambient temperature using synchrotron XRPD. The single crystal of the sample with the largest a lattice parameter had an unusually large mosaic spread, which is the likely origin of the relatively large error bars on the refined occupancies. (b) Variation with a ($=\sqrt{2} \times$ Fe−Fe) of Fe−Se bond lengths (black ●) and the Se−Fe−Se angle of multiplicity two (red ●) (often denoted α) normalized against the smallest value in each series, obtained from NPD at ambient temperatures. The shape of the FeSe$_4$ tetrahedra is similar to that in other iron selenide superconductors and is characterized by being much more squashed in the basal plane than in iron arsenide superconductors (α has a value of about 103°). (c) The correlation of superconducting T_c with refined Fe site occupancy in the selenide layers obtained from refinements against NPD and SCXRD data. (d) Correlation of superconducting T_c with Fe oxidation state obtained from the compositions refined from NPD and SCXRD measurements.

deficiency comes from the results of postsynthetic lithiation described below. The H contents are similar for all samples within the uncertainty, and the Se−H distances of about 3.1 Å between the selenide and hydroxide layers correspond well to those found for weak hydrogen bonding interactions.[17] Thermogravimetric analysis under dry N$_2$ was consistent with dehydration of Li$_{1-x}$Fe$_x$(OH)Fe$_{1-y}$Se commencing at about 350 °C (Figure S7 in the Supporting Information).

The basal lattice parameter a varies linearly with the occupancy of the Fe1 site in the selenide layers which ranges from 0.85(1) to 0.98(1) for the hydrothermally synthesized samples (Figure 2a). This Fe1 occupancy is the only significant compositional and structural difference between samples. Increasing the site occupancy strengthens the Fe−Fe bonding within the FeSe layer, shortening the lattice parameter. Key structural parameters for iron-based superconductors are the Fe−Fe distance in the plane ($=a/\sqrt{2}$), the Fe−E (E = chalcogen or pnictogen) bond length, and the E−Fe−E angles in the FeE$_4$ tetrahedra. For the current compounds the FeSe$_4$ tetrahedra are extremely squashed in the basal plane relative to the more regular tetrahedra found in iron arsenide superconductors,[31] as in FeSe[8] and its intercalates.[17] The Fe−Se distance is rather invariant across the series, and the change in a
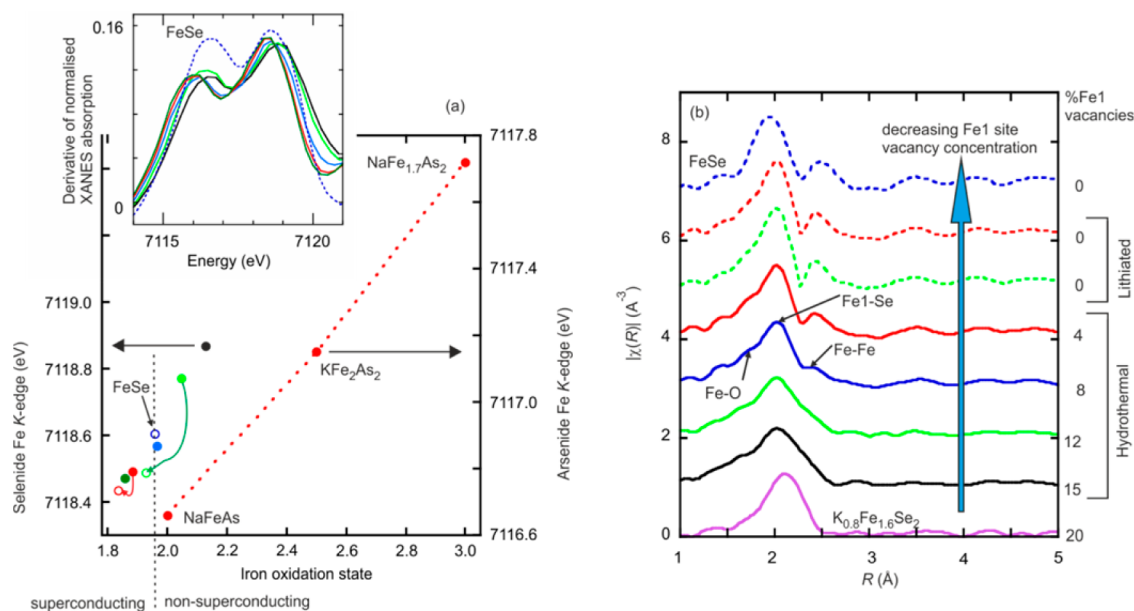
Figure 3. (a) Fe K-edge positions of hydrothermally synthesized $Li_{1-x}Fe_x(OH)Fe_{1-y}Se$ samples (filled colored symbols) plotted as a function of Fe oxidation state obtained from the refined compositions from diffraction data. The curved arrows show the evolution of the edge positions after lithiation (open colored symbols). The inset shows the first derivative of the XANES absorption with the curves carrying the same color as the points in the main figure. FeSe is included for comparison in both figures. The boundary between the superconducting and non-superconducting $Li_{1-x}Fe_x(OH)Fe_{1-y}Se$ samples is indicated. Iron arsenides[34] (red symbols) are included to calibrate the rate of change of edge position with oxidation state. (b) Comparison of the Fe K-edge EXAFS region for a series of hydrothermally synthesized samples (colored solid lines; similar colors for each sample are used in panels a and b) and lithiated samples (colored dotted lines) compared with FeSe and $K_{0.8}Fe_{1.6}Se_2$ (fits are provided in Figures S8 and S9 in the Supporting Information). The EXAFS region is extremely sensitive to the Fe content in the selenide layer (see Tables S3 and S4 in the Supporting Information).

lattice parameter is manifested in the Se−Fe−Se angles (Figure 2b).

NPD data at 295 K and 50 K revealed no evidence for long-range magnetic order. Superconducting samples with the highest Fe1 site occupancies showed a broad reflection at 5.565 Å (Figure S2 in the Supporting Information) which was invariant in intensity with temperature. It may arise from short-range structural ordering of the Li and Fe ions in the hydroxide layers rather than magnetic order. Samples with larger cation vacancy concentrations in the selenide layer (up to 15%) did not exhibit these broad features (Figure S2 in the Supporting Information) nor was there evidence in the SCXRD or NPD data for the long-range iron/vacancy order[10] found in the even more iron deficient (20% vacancies) "2-4-5" $A_{1-x}Fe_{2-2y}Se_2$ ($x \sim y \sim 0.2$) phases.

Semiquantitative energy dispersive analysis of X-rays (EDX) conducted using an FEI Quanta 650 FEG SEM equipped with an Oxford Instruments Aztec EDS detector produced Fe:Se ratios of about 1.1:1 with a 3−5% uncertainty, consistent with the composition obtained from the crystallographic measurements and poorer in iron than the 1.5:1 ratio proposed in ref 20 but in line with refs 21 and 22. Exposure of the hydrothermally synthesized samples to air for 1 week broadened the superconducting transition and reduced the shielding fraction (Figure S5 in the Supporting Information), although the superconducting state was not completely destroyed.

Figure 2c shows that the Fe1 site occupancy controls whether the samples superconduct and the value of T_c. When this occupancy exceeds 95%, the samples superconduct, and T_c increases with increasing site occupancy. In the absence of significant compositional variation in other parts of the structure, a high iron occupancy in the selenide layer

corresponds to a low Fe oxidation state. Computing the mean iron oxidation state from the refined composition for all the hydrothermally synthesized samples probed by NPD and SCXRD shows that for iron oxidation states greater than +2 superconductivity is not observed, while reduction of iron leads to the appearance of superconductivity and T_c increases as the formal oxidation state decreases (Figure 2d).

Preliminary ambient temperature ^{57}Fe Mössbauer spectroscopy measurements on a superconducting sample (Figure S4 in the Supporting Information) showed two paramagnetic doublets, both consistent with Fe(II). The isomer shift of the more intense doublet closely resembles that found in FeSe,[32] and the isomer shift of the minor component is consistent with high-spin Fe^{2+} in the hydroxide layer.[33] Normal state magnetic susceptibility measurements produced a Curie−Weiss type dependence (Figure S5 in the Supporting Information) consistent with a paramagnetic contribution from $S = 2$ moments carried by the Fe^{2+} ions (tetrahedral d^6) on the Li/Fe site in the hydroxide layer. Exposure of samples to laboratory air for 1 week resulted in an increase in the Curie constant consistent with oxidation of these species to Fe^{3+} (tetrahedral d^5), and also led to the partial destruction of superconductivity.

X-ray absorption spectroscopy at the Fe K-edge was used as an additional probe of the Fe oxidation state and the structure. Analysis of the X-ray absorption near edge structure (XANES) region for hydrothermally synthesized samples, representative of the full range of a lattice parameters probed by diffraction methods, produced edge positions spanning 0.34 eV, suggesting oxidation states spanning approximately 0.3 based on the behavior of structurally related materials.[34] A plot of absolute edge position against the Fe oxidation state computed from diffraction measurements produced a linear dependence with a

Table 1. Changes in Lattice Parameters and Refined Site Occupancies on Lithiation from NPD Data

	a (Å)	c (Å)	occ Fe1	occ Li	total Fe
parent A	3.7893(2)	9.2617(6)	0.961(4)	0.812(2)	1.15(1)
daughter A	3.7760(1)	9.3512(2)	1.004(5)	0.837(2)	1.165(5)
parent B	3.8142(3)	9.1882(7)	0.870(5)	0.808(2)	1.064(5)
daughter B	3.7542(1)	9.5859(3)	1.000(8)	0.934(8)	1.07(1)

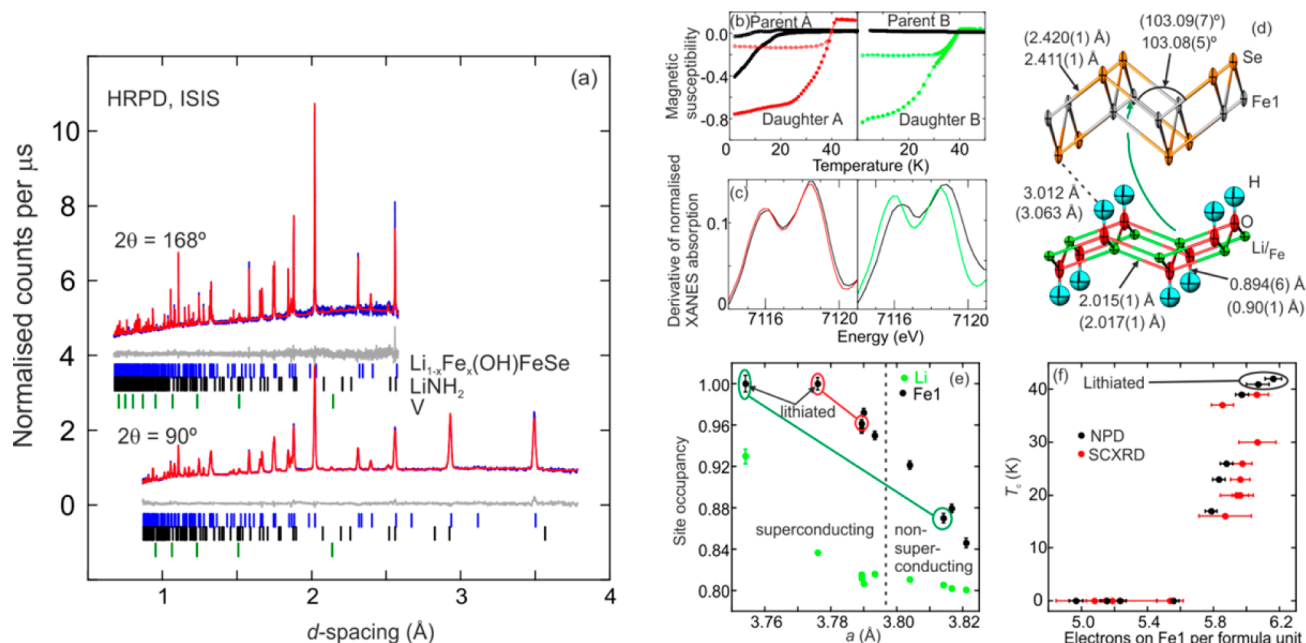**Figure 4.** (a) Rietveld refinement against NPD data of the lithiated product daughter A with a refined composition $Li_{0.84}Fe_{0.16}(OH)FeSe$. The data from the 168° bank are displaced 4 units along the vertical axis. See also Table 1. (b) Enhancing T_c or turning on superconductivity by lithiation of superconducting (parent A) or non-superconducting (parent B) hydrothermally synthesized materials. Daughter A was used for the μSR measurements (Figure 5a). (c) The reduction of Fe effected by lithiation as measured by the shifts in the Fe K-edge absorption energy. (d) Changes in refined structural parameters on lithiation of the superconducting parent A to obtain daughter A; 50% displacement ellipsoids are shown for the lithiated daughter product; refined parameters for parent A are in parentheses. The arrow shows a possible pathway for migration of iron. (e) The correlation between Fe and Li site occupancies and the basal lattice parameter, a, for hydrothermally synthesized and lithiated samples (all results from NPD data). Parent and daughter samples are linked for clarity; in the lithiation of parent A (red line) and parent B (green line) to obtain the daughter products, the increase in the Fe1 site occupancy in the selenide layer is matched by the increasing Li occupancy in the hydroxide layer, so the freely refined iron contents of parent and daughter samples do not vary by more than the uncertainty in the refined values (Table 1). (f) The correlation between superconducting T_c and the average number of valence electrons per $Li_{1-x}Fe_x(OH)Fe_{1-y}Se$ formula unit assigned to the iron atoms in the selenide layers (a parameter that takes into account the iron deficiency in the selenide layer and the iron oxidation state).

gradient similar to that found for related iron arsenides (Figure 3a).[34]

Extended X-ray absorption fine structure (EXAFS) spectra (Figure 3b) showed a sharp sample dependence which (Figures S8 and S9 in the Supporting Information) was determined by the vacancy concentration in the $Fe_{1-y}Se$ layers. The comparison of the EXAFS spectra at around $R = 2-3$ Å for FeSe and the most Fe-poor $Li_{1-x}Fe_x(OH)Fe_{1-y}Se$ sample is similar to the comparison between FeSe and $K_{0.8}Fe_{1.6}Se_2$ (Figure 3b and Figure 2 in ref 35) and in related iron-deficient arsenides.[34] Refinement against the Fe K-edge EXAFS data (Figures S8 and S9 in the Supporting Information) produced ratios of iron on the Fe1 site in the selenide layer and on the $Li/_{Fe}$ site in the hydroxide layer consistent with the values obtained from diffraction, albeit with larger uncertainties (Table S4 in the Supporting Information).

Reductive Lithiation. Analysis of the as-made hydro-thermally synthesized samples shows that superconductivity is observed when the occupancy of the iron site (Fe1) in the selenide layers is high and iron is correspondingly reduced. A subsequent reductive lithiation step using lithium/ammonia

solution was applied to two of the as-made samples (one non-superconducting and the other superconducting) which had been investigated by NPD. The crystal structure of the compounds was maintained, but with a significant increase in the interlayer cell parameter c and a decrease in the basal lattice parameter a (Table 1). When the sample of the non-superconducting hydroxide selenide with 13(1)% vacancies in the $Fe_{1-y}Se$ layers was lithiated, the c lattice parameter increased by 4.3% and the basal a lattice parameter decreased by 1.6%. In both cases the products of the post synthetic lithiation were superconductors with large volume fractions and T_cs exceeding 40 K (Figure 4b), higher than in any of the as-synthesized hydrothermal samples.

Rietveld analysis of NPD data (Figures 4a; Figure S3 and Table S1 in the Supporting Information) from both lithiated samples revealed an increase in the occupancy of the Fe1 tetrahedral site in the selenide layers to 1.00(1) matched by a decrease in the Fe content of the $Li/_{Fe}$ shared site (Table 1, Figure 4e). The refinements constrained the $Li/_{Fe}$ site to be fully occupied so that the Li content of this site increased as its Fe content decreased. Overall Fe contents and the H

occupancy were unconstrained in the refinements, but remained invariant under lithiation within the uncertainty. Figure 4d shows the shortest direct migration pathway for an Fe ion from the hydroxide layer moving to a site in the selenide layer 4.7 Å distant, presumably via the face of the Se_4 tetrahedron forming the target site. This migration may be enabled by the facts that the metal hydroxide layer is relatively flat and the SCXRD measurements show that the $Li/_{Fe}$ ellipsoid is elongated along c and may alternatively be modeled as a split site.[22] XANES measurements of the lithiated samples directly show the Fe K-edge shift arising from the reduction (Figures 3a and 4c), and EXAFS measurements (Figure 3b) show changes in the local structure consistent with the increased Fe content of the Fe1 site revealed by the NPD measurements. The lithiated samples were more air sensitive than the hydrothermally synthesized parents with only vestigial superconductivity evident after 1 week of air exposure (Figure S5 in the Supporting Information).

Characterization of the Superconducting State. Muon-spin rotation (μSR) spectroscopy measurements on the lithiated sample $Li_{0.84}Fe_{0.16}(OH)FeSe$ ("daughter A" in Table 1 and Figure 4a) are depicted in Figure 5a. B_{rms}, the root-mean-square width of the magnetic field distribution experienced by the muon, increases below T_c due to the development of the superconducting vortex lattice, and the behavior of the average field $\langle B \rangle$ shows a diamagnetic response below T_c. These results confirm a superconducting volume fraction above 50%. We extract an in-plane penetration depth, λ_{ab}, of 0.32(3) μm, where the relatively large error takes account of the uncertainty due to field-induced effects associated with the paramagnetic spins in the hydroxide layer. This places $Li_{0.84}Fe_{0.16}(OH)FeSe$ close to the main scaling line in a Uemura plot of T_c against superfluid stiffness $\rho_s = c^2/\lambda_{ab}^2$ (inset to Figure 5a). Figure 5b shows the magnetization as a function of applied magnetic field in a similar lithiated sample with $T_c = 40$ K, as determined by SQUID magnetometry. This shows characteristics of a type II superconductor. The lower critical field H_{c1} is very small, so the Meissner effect is only apparent at lower temperatures, and a significant underlying paramagnetism presumably arises from the Fe^{2+} moments in the hydroxide layer. The inset to Figure 5b shows the approximate evolution of H_{c1} with temperature, as deduced from the susceptibility, calculated from the magnetization data in the main figure. A correction for the effect of the paramagnetic Fe^{2+} centers in the hydroxide layer (Figure S10 in the Supporting Information) yields no evidence for the upper critical field H_{c2}, so we deduce that $\mu_0 H_{c2} > 7$ T, in line with the behavior of other iron-based superconductors.

CONCLUSIONS

In conclusion we have demonstrated that hydrothermal synthesis under appropriate conditions yields $Li_{1-x}Fe_x(OH)$-$Fe_{1-y}Se$ with $x \sim 0.2$ and with a highly variable y that provides insight into the controlling parameters for superconductivity in iron selenides. For $0.05 < y < 0.15$, the samples are non-superconducting, but as the Fe deficiency, y, decreases and Fe is reduced, superconductivity emerges. Furthermore, superconductivity with the highest T_cs and shielding fractions can be turned on by reductive lithiation to intentionally reduce y to zero: additional Li displaces some Fe ions from the hydroxide layer "reservoir" which migrate to completely fill the Fe site vacancies in the selenide layers, and the mean oxidation state of iron is reduced below +2. Figure 4f plots T_c (defined to be 0 K for non-superconductors) against the number of 3d electrons
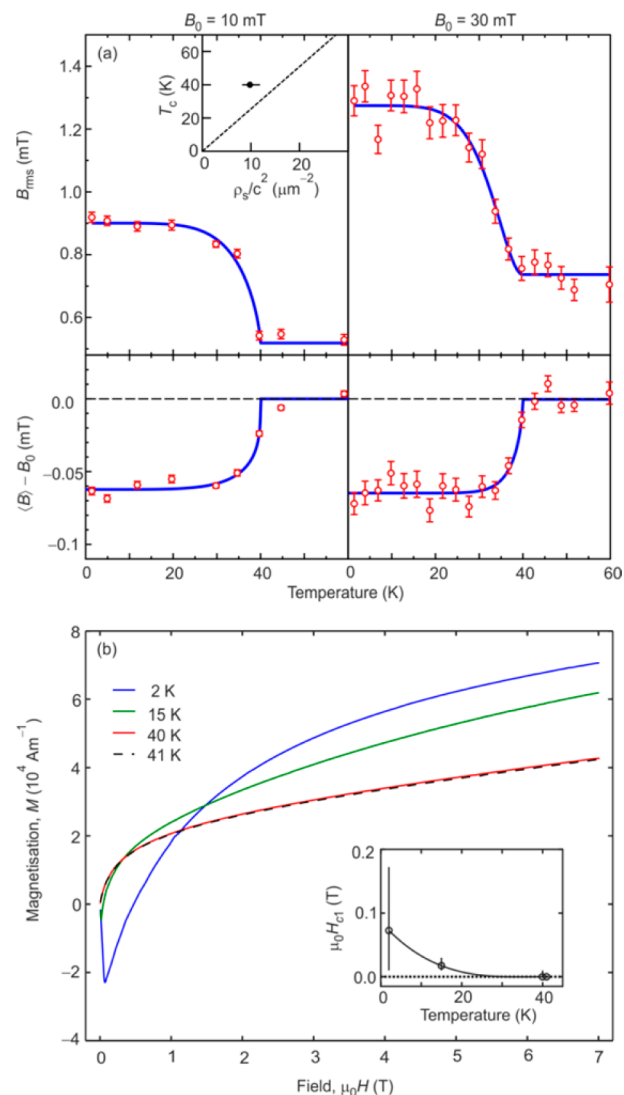

Figure 5. (a) The results of transverse-field muon-spin rotation spectroscopy on the lithiated sample "daughter A" (see Figure 4; Table 1). While the diamagnetic response, measured by $\langle B \rangle - B_0$, which reflects the superconducting state only, is invariant with the applied transverse field, B_0, B_{rms} increases with B_0 even in the normal state, which shows that there is a field-dependent contribution to the magnetic field distribution experienced by the muon that is likely due to the paramagnetic background originating from the Fe^{2+} ions in the hydroxide layer. The different contributions to B_{rms} act in quadrature ($B_{rms}^2 = \sum b_{rms}^2$). From the proportionality between the superconducting contribution to B_{rms} and $1/\lambda_{ab}^2 = \rho_s/c^2$, where $\lambda_{ab} = 3^{1/4}\lambda$ is the in-plane penetration depth and ρ_s is the superfluid stiffness, we extract $\lambda_{ab} = 0.32(3)$ μm. (b) Magnetization as a function of magnetic field for a lithiated sample with $T_c = 40$ K. In the inset, open circles illustrate the field at which the calculated susceptibility is equal to zero, bars illustrate the approximate width in H of the transition from the Meissner state to the vortex lattice state, and the dashed line is a guide to the eye.

associated with the iron atoms in the selenide layer per $Li_{1-x}Fe_x(OH)Fe_{1-y}Se$ formula unit, assuming the +2 oxidation state for Fe ions in the hydroxide layers. This quantity takes into account both the Fe1 site occupancy and the iron oxidation state. T_c increases smoothly with increasing Fe electron count per formula unit once a threshold value is reached. These results provide a bridge between the two phases present in alkali metal iron selenide systems such as

$K_{0.8}Fe_{1.6}Se_2$[9] where high Fe site occupancies and Fe oxidation states slightly below +2 are found in portions of the samples which show superconductivity, but the bulk of the sample is a magnetic insulator with a 20% Fe deficiency and crystallographic ordering of the ensuing vacancies.[10] This underlines and quantifies the importance of structure and electron count in controlling superconductivity in iron selenide superconductors.

■ ASSOCIATED CONTENT

ⓈSupporting Information

Crystallographic data in CIF format. Summary of refined structural paramaters, Rietveld refinements against neutron powder diffraction data, Mössbauer spectrum, effects of air exposure on superconducting and magnetic properties, SEM analysis, thermogravimetric analysis, analysis of EXAFS data, and high field magnetometry. This material is available free of charge via the Internet at http://pubs.acs.org. Crystallographic data have been deposited at the FIZ, Karlsruhe with accession number 428281 (http://www.fiz-karlsruhe.de/icsd.html).

■ AUTHOR INFORMATION

Corresponding Author
*E-mail: simon.clarke@chem.ox.ac.uk.

Notes
The authors declare no competing financial interest.

■ ACKNOWLEDGMENTS

■ REFERENCES

(1) Kamihara, Y.; Watanabe, T.; Hirano, M.; Hosono, H. *J. Am. Chem. Soc.* **2008**, *130*, 3296−3297.
(2) Rotter, M.; Tegel, M.; Johrendt, D. *Phys. Rev. Lett.* **2008**, *101*, 107006.
(3) Canfield, P. C.; Bud'ko, S. L.; Ni, N.; Yan, J. Q.; Kracher, A. *Phys. Rev. B* **2009**, *80*, 060501(R).
(4) Wright, J. D.; Lancaster, T.; Franke, I.; Steele, A. J.; Möller, J. S.; Pitcher, M. J.; Corkett, A. J.; Free, D. G.; Parker, D. R.; Pratt, F. L.; Baker, P. J.; Clarke, S. J.; Blundell, S. J. *Phys. Rev. B* **2012**, *85*, 054503.
(5) Iimura, S.; Matsuishi, S.; Sato, H.; Hanna, T.; Muraba, Y.; Kim, S. W.; Kim, J. E.; Takata, M.; Hosono, H. *Nat. Commun.* **2012**, *3*, 943.
(6) Johrendt, D. *J. Mater. Chem.* **2011**, *21*, 13726−13736.
(7) Hsu, F.-C.; Luo, J.-Y.; Yeh, K.-W.; Chen, T.-K.; Huang, T.-W.; Wu, P. M.; Lee, Y.-C.; Huang, Y.-L.; Chu, Y.-Y.; Yan, D.-C.; Wu, M.-K. *Proc. Natl. Acad. Sci. U.S.A.* **2008**, *105*, 14262−14264.
(8) McQueen, T. M.; Huang, Q.; Ksenofontov, V.; Felser, C.; Xu, Q.; Zandbergen, H.; Hor, Y. S.; Allred, J.; Williams, A. J.; Qu, Q.; Checkelsky, J.; Ong, N. P.; Cava, R. J. *Phys. Rev. B* **2009**, *79*, 014522.
(9) Guo, J.-G.; Jin, S.-F.; Wang, G.; Wang, S.-C.; Zhu, K.-X.; Zhou, T.-T.; He, M.; Chen, X. L. *Phys. Rev. B* **2010**, *82*, 180520.
(10) Bacsa, J.; Ganin, A. Y.; Takabayashi, Y.; Christensen, K. E.; Prassides, K.; Rosseinsky, M. J.; Claridge, J. B. *Chem. Sci.* **2011**, *2*, 1054−1058.
(11) Pomjakushin, V. Y.; Pomjakushina, E. V.; Krzton-Maziopa, A.; Conder, K.; Shermadini, Z. *J. Phys: Condens. Matter* **2011**, *23*, 156003.
(12) Texier, Y.; Deisenhofer, J.; Tsurkan, V.; Loidl, A.; Inosov, D. S.; Friemel, G.; Bobroff, J. *Phys. Rev. Lett.* **2012**, *108*, 237002.
(13) Shoemaker, D. P.; Chung, D. Y.; Claus, H.; Francisco, M. C.; Avci, S.; Llobet, A.; Kanatzidis, M. G. *Phys. Rev. B* **2012**, *86*, 184511.
(14) Carr, S. V.; Louca, D.; Siewenie, J.; Huang, Q.; Wang, A. F.; Chen, X. H.; Dai, P. C. *Phys. Rev. B* **2014**, *89*, 134509.
(15) Ying, T. P.; Chen, X. L.; Wang, G.; Jin, S. F.; Zhou, T. T.; Lai, X. F.; Zhang, H.; Wang, W. Y. *Sci. Rep.* **2012**, *2*, 426.
(16) Ying, T.; Chen, X.; Wang, G.; Jin, S.; Lai, X.; Zhou, T.; Zhang, H.; Shen, S.; Wang, W. *J. Am. Chem. Soc.* **2013**, *135*, 2951−2954.
(17) Burrard-Lucas, M.; Free, D. G.; Sedlmaier, S. J.; Wright, J. D.; Cassidy, S. J.; Hara, Y.; Corkett, A. J.; Lancaster, T.; Baker, P. J.; Blundell, S. J.; Clarke, S. J. *Nat. Mater.* **2013**, *12*, 15−19.
(18) Scheidt, E.-W.; Hathawar, V. R.; Schmitz, D.; Dunbar, A.; Scherer, W.; Mayr, F.; Tsurkan, V.; Deisenhofer, J.; Loidl, A. *Eur. Phys. J. B* **2012**, *85*, 279−283.
(19) Sedlmaier, S. J.; Cassidy, S. J.; Morris, R.; Drakopoulos, M.; Reinhard, C.; Moorhouse, S. J.; O'Hare, D.; Manuel, P.; Khalyavin, D.; Clarke, S. J. *J. Am. Chem. Soc.* **2014**, *136*, 630−633.
(20) Lu, X. F.; Wang, N. Z.; Zhang, G. H.; Luo, X. G.; Ma, Z. M.; Lei, B.; Huang, F. Q.; Chen, X. H. *Phys. Rev. B* **2013**, *89*, 020507(R).
(21) Lu, X. F.; Wang, N. Z.; Wu, H.; Wu, Y. P.; Zhao, D.; Zeng, X. Z.; Luo, X. G.; Wu, T.; Bao, W.; Zhang, G. H.; Huang, F. Q.; Huang, Q. Z.; Chen, X. H. *Nat. Mater.* **2015**, DOI: 10.1038/nmat4155.
(22) Pachmayr, U.; Nitsche, F.; Luetkens, H.; Kamusella, S.; Brückner, F.; Sarkar, R.; Klauss, H.-H.; Johrendt, D. *Angew. Chem., Int. Ed.* **2015**, *54*, 293−297.
(23) Ziemkiewicz, P. F.; O'Neal, M.; Lovett, R. J. *Mine Water Environ.* **2011**, *30*, 141−150.
(24) Palatinus, L.; Chapuis, G. *J. Appl. Crystallogr.* **2007**, *40*, 786−790.
(25) Betteridge, P. W.; Carruthers, J. R.; Cooper, R. I.; Prout, K.; Watkin, D. J. *J. Appl. Crystallogr.* **2003**, *36*, 1487−1487.
(26) Coelho, A. A. *TOPAS Academic, Version 5*; Coelho Software: Brisbane, Australia, 2012.
(27) Blundell, S. J. *Magnetism in Condensed Matter*; Oxford University Press: Oxford, U.K., 2001.
(28) Ravel, B.; Newville, M. *J. Synchrotron Radiat.* **2005**, *12*, 537−541.
(29) Minagawa, T. *Mem. Osaka Kyoiku Univ., Ser. III* **1994**, *43*, 39−45.
(30) Sears, V. F. *Neutron News* **1992**, *3*, 29−37.
(31) Lee, C. H.; Kihou, K.; Iyo, A.; Kito, H.; Shirage, P. M.; Eisaki, H. *Solid State Commun.* **2012**, *152*, 644−648.
(32) Lindén, J. K. M.; Rautama, E.-L.; Karppinen, M.; Yamauchi, H. *Hyperfine Interact.* **2012**, *208*, 133−136.
(33) Maddock, A. G. *Mössbauer Spectroscopy*; Horwood Publishing: Chichester, U.K., 1997.
(34) Cassidy, S. J.; Ramos, S.; Clarke, S. J. *Z. Anorg. Allg. Chem.* **2014**, *640*, 2889−2896.
(35) Iadecola, A.; Joseph, B.; Simonelli, L.; Puri, A.; Mizuguchi, Y.; Takeya, H.; Takano, Y.; Saini, N. L. *J. Phys.: Condens. Matter* **2012**, *24*, 115701.